A Statistical Study of the Global Structure of the Ring Current.

A. M. Jorgensen[1], H. E. Spence[2], W. J. Hughes[2], H. J. Singer[3]

Short title: GLOBAL STRUCTURE OF THE RING CURRENT

[1]Los Alamos National Laboratory, Los Alamos, NM, USA

[2]Center for Space Physics, Boston University, MA, USA

[3]NOAA Space Environment Center, Boulder, CO, USA

Abstract.

In this paper we derive the average configuration of the ring current as a function of the state of the magnetosphere as indicated by the *Dst* index. We sort magnetic field data from the Combined Release and Radiation Effects Satellite (CRRES) by spatial location and by the *Dst* index in order to produce magnetic field maps. From these maps we calculate local current systems by taking the curl of the magnetic field. We find both the westward (outer) and the eastward (inner) components of the ring current. We find that the ring current intensity varies linearly with *Dst* as expected, and that the ring current is asymmetric for all *Dst* values. The azimuthal peak of the ring current is located in the afternoon sector for quiet conditions, and near midnight for disturbed conditions. The ring current also moves closer to the Earth during disturbed conditions. We are able to recreate the *Dst* index by integrating the magnetic perturbations caused by the ring current. We find that we needed to apply a 20 nT offset to *Dst*, and assume a perfectly conducting Earth to obtain an optimal agreement between the computed and the observed *Dst*. We interpret the 20 nT offset as the magnetic field generated by the quiet time ring current used as baseline in computing *Dst*.

Introduction

Using space-based magnetic field and particle sensors a number of empirical models or maps of the magnetosphere have been constructed. The first comprehensive magnetic field map was created by *Sugiura et al.* [1971] using OGO 3 and 5 data. They found significant variations from the internal magnetic field, even deep in the inner magnetosphere, inside of 3 R_E, for disturbed times as well as for quiet times. This suggested that a significant ring current was present for all levels of activity, and that the storm-time ring current is merely an intensification of a quiet-time ring current. Numerous magnetic field measurements have since been produced [e.g. *Tsyganenko*, 1987; *Mead and Fairfield*, 1975; *Olson and Pfitzer*, 1974]. Such models are generally analytically derived and then fitted to a set of measurements. They have proven immensely useful in providing contextual information for event studies, but suffer from only being able to represent a limited set of configurations. In fact, most models do not adequately represent the magnetic field in the near-Earth region where they are expected to be reliable. *Reeves et al.* [1996] showed that models even have difficulties in mapping geostationary orbit to the auroral zone, a region of the magnetosphere where the dipole component is still quite strong. This difficulty is partly attributable to oversimplified ring current representations in these models.

The asymmetry of the low-latitude H component associated with magnetic storms has long been known to be asymmetric [*Chapman*, 1918; *Akasofu and Chapman*, 1964; *Crooker and Siscoe*, 1971]. Although the asymmetry originally was attributed to

ionospheric currents [*Chapman*, 1918], later work suggested that it could instead be due to an azimuthally asymmetric ring current [*Kirkpatrick*, 1952; *Fejer*, 1961; *Akasofu and Chapman*, 1964]. *Crooker and Siscoe* [1981] proposed, based in part on simulation results by *Harel et al.* [1981], that the asymmetry is instead caused by a mismatch between region 1 and region 2 currents. This mismatch arose as the divergence of the Hall current at the conductivity discontinuity at the poleward edge of the auroral oval. They contended that there is no substantial asymmetric ring current.

Later studies used in-situ data without a model fit to try to determine the magnetic field configuration, and thus the current patterns in the inner magnetosphere. *Ijima et al.* [1990] used AMPTE/CCE data to study the currents in the equatorial plane of the inner magnetosphere between L=4.0 R_E and L=8.8 R_E. They found a westward flowing azimuthal current with a pronounced noon-midnight asymmetry for moderately disturbed conditions ($-70\,nT \leq Dst \leq -20\,nT$). The currents at midnight were 2 to 3 times larger than the currents at noon. They found no dawn-dusk asymmetry in the azimuthal currents.

Another technique used for inferring magnetospheric currents relies on measured gradients in the plasma pressure. By assuming that the plasma and fields are in magnetostatic equilibrium, currents can be computed from knowledge of pressure gradients. The radial plasma pressure profiles in the midnight magnetosphere have been studied by *Lui et al.* [1987], *Spence et al.* [1989], and *Lui and Hamilton* [1992]. All three papers found a pressure increasing Earthward until approximately 3 R_E, where it peaked and then decreased towards the Earth. This implied a two-component ring

current, with westward current outside of pressure peak and eastward current inside of the pressure peak. *Lui et al.* [1987] studied several magnetic storms, and found that the plasma pressure generally exhibits a peak in the vicinity of 3 R_E, for quiet times, as well as for storm times. They used the pressure profiles to derive current densities and found quiet time currents typically $2\,nA/m^2$ and $1\,nA/m^2$ for the inner and outer current during quiet times, and typically $3\,nA/m^2$ to $5\,nA/m^2$ for storm times. The statistical study by *Lui and Hamilton* [1992] showed similar results. The eastward current peaked near $2.5\,R_E$, and most of the current was carried between 2 and 3 R_E. The westward current peaked between 4 and 8 R_E, with the majority of the current being carried in that region.

More recently *De Michelis et al.* [1997] produced a picture of the average ring current again based on particle measurements from the CHEM instrument on AMPTE/CCE for 4 different local time sectors. They found both the eastward (inner) and the westward (outer) component of the ring current. The pressure peak is located near 4.5 R_E, which is at a somewhat greater distance than in other studies. The total eastward current was slightly smaller than the total westward current, resulting in a net westward current. They also observed a strong asymmetry in the current, similar to that observed by *Ijima et al.* [1990], with the current near 23 MLT being 2 to 3 times stronger than the current on the dayside.

Most recently *Nakabe et al.* [1997] used DE-1 magnetic field data to create an empirical map of the magnetic field in the inner magnetosphere between $2\,R_E$ and $4.6\,R_E$. They did not directly calculate current maps but instead estimated the current

structure from visual inspection of the magnetic field maps. They found evidence for both a westward (outer) and an eastward (inner) current. The westward current was found to be symmetrically peaked near midnight, both during quiet times and during more disturbed times. However, the eastward current was only evident on the dayside, and appeared very intense, up to 50 nA/m^2. As they note, this is in conflict with previous studies.

Although there appears to be general agreement as to the existence of the asymmetric ring current, its location and magnitude as a function of geomagnetic activity is still debated. In this paper we will examine the location, strength, and asymmetry of the ring current for different levels of geomagnetic activity. We then compare these results with the past results mentioned above.

Data set and analysis

For this study we make use of the magnetic field data from the fluxgate magnetometer on the CRRES satellite. The fluxgate magnetometer on CRRES has been thoroughly described by *Singer et al.* [1992]. In this paper we use 1-min averaged data.

CRRES was launched on July 25th, 1990, and was operational until October 1991 when a critical power subsystem failed. The CRRES orbit was initially 350 km altitude by 6.3 R_E geocentric, with an orbital inclination of 18°, giving it a maximum range in magnetic latitude of ±29°. The orbital period was 10.5 hours at launch, decreasing to 9.5 hours by October 1991. Our data set only includes data while CRRES was

at a radial distance greater than 2 R_E and does not include data from the so called "precession orbits" when CRRES was maneuvering.

During the CRRES period there were a number of large magnetic storms, which provides data for the study of the active ring current. The distribution of *Dst* measurements for times when good magnetic field measurements were obtained (see explanation below) is shown in Figure 1. The figure also shows the scaled distribution of *Dst* for the years 1970 to 1995. It can be seen that the CRRES period had a somewhat larger probability of smaller (more intense) *Dst*'s, so the period represents a more active than average ring current in a statistical sense.

In order to study the *Dst* variation of the ring current we sort the data into different *Dst* ranges. The largest *Dst* value measured was 53 nT, and the smallest was -295 nT. Table 1 lists the number and fraction of data points in adjacent 30-nT-wide intervals. It shows that greater than 96% of the data occur for *Dst* values between -90 nT and 30 nT and each 30 nT wide interval in that range contains at least 7% of the data, thus providing a good basis for statistical analysis. For part of this paper, we will consider all the Dst ranges listed in Table 1; other sorting strategies and intervals will be discussed later as appropriate.

Figure 1.

Table 1.

The spatial coverage of CRRES is shown in Figure 2. The figure shows the number of minutes CRRES spent in different spatial regions during times when *Dst* was in certain intervals. Panels a,c, and e show the L-MLT coverage for the *Dst* intervals $[-60;-30]$, $[-30;0]$, and $[0;30]$ nT. Each spatial bin is 0.2 R_E by one hour of magnetic local time (MLT). Panels b, d, and f show noon, midnight, dusk and dawn cuts through

the three-dimensional coverage. The coordinate system used for these plots, as well as all following analysis is the Solar Magnetic (SM) coordinate system. This coordinate system was chosen because it is simple to use and because we expect the ring current location to be constant in this coordinate system for a given magnetospheric state, independent of other parameters, such as dipole tilt, universal time and season. Each bin is 0.2 R_E by 0.2 R_E by six hours of MLT.

We assume the ring current to be symmetric around the equatorial (z=0) plane so each data point is represented twice: once at the actual measurement location, and once at the mirror point around the equatorial plane. From this point onwards in the paper we will use this symmetric property of the data to maximize data coverage and to aid in visualization. When we compute residence times in a bin, we include both the sum of the residence times in a bin and its symmetrically located bin. Table 2 shows the average and median coverage (in minutes) for different *Dst* intervals. Because the actual spatial coverage was not symmetric around the equatorial plane, the average and median times in any bin would be reduced to about two thirds (not one half) of the stated values if we had not adopted the symmetry argument.

Figure 2.

Table 2.

We used these data to study the global structure and dynamics of the ring current magnetic field. If we are able to sort the data by location, and *exact* state of the system, this method gives us an *exact* representation of the configuration of the ring current for the different states sampled. In this paper we used *Dst* as the state variable. While *Dst* does not define the exact state of the magnetosphere, it is probably the best, most available, and most extensively used index for ring current studies. Thus, using *Dst* as

the magnetospheric state variable we sorted the radial (B_R) and axial (B_Z) components of the magnetic field into a three-dimensional cylindrical grid with radial and axial bin separation of 0.2 R_E and varying azimuthal bin size. In order to avoid aliasing due to the large variation of the total magnetic field with radial distance, we detrended the measured field using an internal field model (IGRF). The precise nature of the internal field model is unimportant as it does not contribute to the ring current that we are measuring. The field shown and analyzed throughout this paper are the detrended fields. In addition, some smoothing and interpolation were performed in specific cases. These instances are described as encountered later in the paper.

In each bin the average magnetic field component was calculated in addition to the number of data points that contributed to that bin. Because of symmetry, when the radial component of the magnetic field is added to values from its mirror bin, they must be reflected to account for the sign change accross the equatorial plane. Figure 3 shows the average radial magnetic field after performing this mirror correction, while Figure 4 shows the average axial magnetic field values for four six-hour MLT interval and five *Dst* intervals.

Figure 3.

Figure 4.

From the data shown in Figures 3 and 4 we calculate the currents equivalent to the magnetic field variations. Calculating current requires taking spatial derivatives of the binned magnetic field. To minimize the statistical scatter in the field maps, the data is first smoothed. Then in order to minimize holes in the field maps, missing data is filled in as described below. We bin the data as described above, but in order to improve statistics, we include in each 0.2 by 0.2 R_E bin all the data from a 0.6 by 0.6 R_E region

centered on that bin. This process smooths the data and also fills in some bins where data are missing. After this we smooth the data again with a 3×3 box-car in the R-Z plane. That is, for each pixel where data are available, we replace the value, v, in that pixel, by the value s, where

$$s = \frac{\sum_A v_i n_i}{\sum_A n_i}, \tag{1}$$

where A is the pixel itself and the surrounding eight pixles, v_i is the average in a bin, and n_i is the number of data points that contributed to a bin. This smoothing operation does not fill in data for which there was none in the original array, as opposed to the original 0.6×0.6 binning scheme.

The final operation performed on the binned data is "patching". The patching operation is more complicated in that it is designed to interpolate values for pixels that have missing values, but for which the surrounding pixels have values. The eight pixels surrounding the pixel to be interpolated are examined. To patch an empty pixel, we require that at least two of the eight pixels contain data. Furthermore, we required that the surrounding pixels with data were symmetrically located around the pixel to be patched. We did this by taking the sum of the R and Z bin coordinates relative to the pixel to be patched, of the surrounding pixels. These relative bin coorindates will be either -1, 0, or 1. We then require the sum of these coordinates to be -1, 0, or 1 for the the R, and Z direction separately. In this way we ensure that we only interpolate if the pixels we use for the interpolation are distributed somewhat symmetrically around

the center pixel. Once it has been established that the pixel can be interpolated, its null value is replaced with the value calculated from Eq. 1, where the sum is again over those of the eight neighbor pixels that have values.

In summary we apply one smooth operation to the data in Figures 3 and 4, and then iterate the patching algorithm until no more pixels can be interpolated. Before patching, the total number of pixels with data was 10492. The patching algorithm adds only 123 pixels, all of which are internal to regions that already contain data. Next we calculate the azimuthal current from these data. The current is defined as

$$j_\phi = \frac{1}{\mu_0}\left(\frac{dB_R}{dz} - \frac{dB_Z}{dr}\right). \tag{2}$$

Since our data are binned into discrete spatial arrays, we use a finite difference expression to calculate the derivatives. The current calculated in a given pixel (j,i) is then

$$j_\phi(j,i) = \frac{1}{\mu_0}\left(\frac{B_R(j,i+1) - B_R(j,i-1)}{Z(j,i+1) - Z(j,i-1)} - \frac{B_Z(j+1,i) - B_Z(j-1,i)}{R(j+1,i) - R(j+1,i)}\right). \tag{3}$$

The current calculated from equation 3 is shown in Figure 5. **Figure 5.**

Results

Figure 5 shows the calculated current patterns and several expected features are prominent. First, there is an eastward-directed (inner) component to the ring current, shown in red, as well as a westward-directed (outer) component shown in blue. These two currents are consistent with a ring current plasma pressure peak located at

approximately 3.5 R_E, according to the magnetohydrostatic equation $\vec{j} \times \vec{B} = -\nabla p$. It follows from this equation that the ring current must change sign as the pressure gradient changes sign across the pressure peak. The figure also demonstrates that the currents are more intense (more intense blue and red colors) for smaller Dst values. This is consistent with the Dst index being a measure of the intensity of the ring current. Both of these characteristics (an inner and outer ring current, and their overall intensity changes with Dst) are in good agreement with previous studies.

Another prominent feature evident in Figure 5 is the strong local time asymmetry of the ring current. As noted in the introduction this asymmetry has been seen in previous studies, however there have been large discrepancies as to its properties. We note in our analysis that particularly the eastward currents, but also the westward currents, appear more intense near dusk and midnight than they do near dawn and noon. In the following we will further quantify the variation of the ring current intensity, its asymmetry, and it's location, and compare these to the differing results from previous studies.

Figure 6 shows the average azimuthal current density as a function of radial distance in the equatorial plane for four different MLT sectors. These were calculated for each radial bin in Figure 5, as the average of the center six pixels (within 0.6 R_E of the equatorial plane), weighted by the number of contributing data points. As in Figure 5 the current densities are larger in the dusk and midnight sectors than at dawn, and significantly larger than in the noon sector. The increase of the current densities with decreasing Dst is clear in all local time sectors. We can also see that the westward (outer) component, possessing negative current values, shows a larger variation of the

current density with *Dst* than the eastward (inner) component.

The pressure peak of the ring current is indicated by the zero crossing of the current profiles, and appears to be located between 3 and 4 R_E. This result agrees qualitatively well with those of *Lui et al.* [1987]. Both data sets put the ring current peak near 3 R_E, but the currents of *Lui et al.* [1987] are smaller by a factor of 2 to 3 than those we derive for similar *Dst* conditions. *De Michelis et al.* [1997] place the ring current peak near 4.5 R_E and also observe current densities that are smaller than the ones we observe, although a direct comparison is difficult since their data are sorted by *AE*. The peak of the westward current is located at or beyond 4 R_E, except for the most disturbed cases. This is consistent with *Nakabe et al.* [1997], who deduce from their magnetic field profiles that the peak current is located outside their coverage radius of 4.6 R_E.

Figure 6.

In Figure 7, equatorial azimuthal currents as a function of MLT are plotted for different radial distances and *Dst* values. The ring current asymmetry can be seen as an enhanced current density in the dusk sector. It also appears that the asymmetry is larger for more intense storm-time *Dst* conditions, than for the more quiet *Dst* conditions. The asymmetry is larger in the portions of the ring current that are closer to the Earth. *Ijima et al.* [1990] calculated the azimuthal currents as a function of MLT, and also found a significant nightside peak. Although they interpret their results as a midnight centered current, their Figure 5 also appears to be consistent with a current that is skewed towards the dusk side. This would put our result and their result in better agreement.

Figure 7.

Discussion

Ring current strength variation with Dst

To establish a clear quantitative relation between the strength of the westward and eastward currents and Dst, we calculated the total azimuthal average ring current in both the inner and outer ring currents separately. This was done by first calculating the average current pattern over all azimuth locations for each Dst range, and then summing the total of all positive (eastward) currents and negative (westward) currents. To be included in the sum, we further required that bin centers for the positive (negative) current must lie within (outside of) radial distances of $4\,R_E$ ($3\,R_E$). To better reveal the relationship with Dst, we used a sliding 30-nT-wide window centered on Dst values 10 nT apart, ranging from center values of +45 nT to −145 nT.

The results are shown in Figure 8, where the solid line represents the westward (outer) total ring current, and the dotted line is the eastward (inner) total ring current. It can be seen that between approximately -120 nT and 0 nT both currents vary approximately linearly with Dst. Overplotted are straight line fits to the linear portions of both curves, which for the westward (outer) current is given by

$$I_{west} = -0.77\,MA + 0.035\,MA/nT \times Dst, \tag{4}$$

and for the eastward (inner) current given by

$$I_{east} = 0.22\,MA - 0.0045 MA/nT \times Dst. \tag{5}$$

Figure 8 shows that this same linear trend does not hold for either the very high ($> 10\,nT$) or the very low ($< -120\,nT$) values of Dst. These variations can be caused by the smaller data set available at extreme Dst values. A decrease of the absolute value of the current can be caused when spatial coverage decreases, since in such cases we will be missing part of the current when we only integrate over pixels that have data. An increase in the absolute value of the current can also be caused. The reason for this is that we integrate only over either positive of negative current densities. As the noise level increases, so will the average value of the current density included. Therefore the behavior of the curves for extreme values of Dst should be considered artifacts of the method.

It is interesting to note from equations 4 and 5 that the currents do not intersect the Dst axis at 0 nT. The westward current is zero at Dst=22 nT, while the eastward curret is zero at Dst=49 nT. If we decide to trust equation 4 more due to its steeper angle with the Dst axis, we see that there is an offset in the Dst index, so that Dst=0 actually conresponds to a ring current that would create a 20 nT depression. This is probably due to the normalization of the Dst index, which is done using "quiet" day as a baseline. We are suggesting that a quiet day may actually in the average correspond to a ring current that produces a 20 nT disturbance.

Figure 8.

Radial position of the ring current

We define the mean radial location of the ring current, r_m, as the integral over location, weighted by the current density at that position,

$$r_m = \frac{\int_A r\, j(\vec{r})}{\int_A j(\vec{r})}. \tag{6}$$

For the westward (outer) current, A includes those pixels whose centers are at least 3 R_E from the center of the Earth, and have negative current density. For the eastward (inner) current, A includes those pixels whose centers are at most 4 R_E from the center of the Earth, and have positive current density. Figure 9 shows the mean radial distances of the eastward and westward ring currents. These locations were calculated from equation 6 using the same data as for calculating the total currents in Figure 8. As with the total current, the position of the peak currents varies approximately linearly between -120 nT and 0 nT. The position of the westward (outer) current is approximately described by the expression $r_w = 5.81\, R_E + 0.0073\, R_E/nT \times Dst$, while the position of the eastward (inner) current is $r_e = 2.90\, R_E + 0.00084\, R_E/nT \times Dst$. The peak of the westward (outer) current moves inward approximately 0.9 R_E as Dst decreases from 0 nT to -120 nT, while the eastward (inner) current essentially does not move (0.1 R_E) for the same decrease.

Figure 9.

Asymmetry of the ring current

The asymmetry of the ring current is determined by two parameters; the position of the peak of the ring current, and the asymmetry of the ring current at that location (which we will call the peak asymmetry). There are a number of different ways to define the peak and the asymmetry. We investigated two such ways, and found that they yielded similar results. The simplest method is to first calculate the current, $I(\phi)$, at

every local time interval by the method used to generate Figure 8, and then designate the local time interval with the largest current as the ring current peak, $I(\phi_{peak})$. Next the asymmetry of the peak current, α, is calculated as

$$\alpha = \frac{1}{2}\frac{I(\phi_{peak}) - I(\phi_{peak}+\pi)}{I(\phi_{peak}) + I(\phi_{peak}+\pi)}. \tag{7}$$

Another method is to compare current densities directly. This is done by calculating the asymmetry between all pairs of pixels, using an expression similar to equation 7), on opposite sides of the Earth, and then averaging that asymmetry over each magnetic local time slice. The peak is located in the slice where this average asymmetry is largest, and the peak asymmetry is that average asymmetry. In calculating the asymmetry of the westward (outer) current, we use only those pairs of pixels that are located no closer than $3\,R_E$ from the center of the Earth, and where both pixels in the pair have negative current. For the asymmetry of the eastward (inner) current we required pixels to be located no more than $4\,R_E$ from the center of the Earth, and have positive current. As the data set we use a 12 hour MLT average in 24 MLT bins.

We find that that the two definitions yield similar results, and so show only the results of the second approach, the current density asymmetry. Figure 10 shows the MLT location of the peak plotted as a function of *Dst*. The solid line shows the westward (outer) current, and the dotted line shows the eastward (inner) current. Figure 10 shows that the peak of the westward (outer) current moves from near 15 MLT at *Dst* of 0 nT, to near midnight as *Dst* decreases to -100 nT. Between -100 nT and

0 nT there is a moderate amount of scatter, nevertheless the peak clearly shifts toward midnight as *Dst* decreases. As noted in Figure 8, departures of this trend at both very high and very low *Dst* are attributable to inadequicies in the data and to details of our analysis, and are not considered further. Finally we note that for the eastward (inner) current there is no clear trend, regardless of the *Dst* range.

Figure 11 shows that the asymmetry of the westward (outer) current is 10-20%, while the asymmetry of the eastward (inner) current is slightly larger at 15-25%. No clear trend with *Dst* is evident in the asymmetry. The calculation of the asymmetry was also repeated with 8 hour averages. We found similar results for the peak location, but with the asymmetry of the eastward (inner) current being slightly larger at 20-30%. It should be noted that the asymmetry measure does not compare directly to those quoted by *Ijima et al.* [1990] and *De Michelis et al.* [1997]. However Figure 7 shows that for a given *Dst* range, the largest current observed is 2 to 3 times larger than the smallest current observed, in good agreement with previous measurements.

Figure 10.

Figure 11.

A linear expression that quantifies the position of the asymmetry peak shown in Figure 10 between -100 nT and 0 nT, is

$$\phi_{peak} = 16\,Hr - \frac{Dst}{10\,\frac{nT}{Hr}} \tag{8}$$

such a motion of the ring current is consistent with the idea that the ring current source is in the tail. During more active times we would expect the ring current to be more intense in the vicinity of the source. In addition, in the midnight region, the tail current

and the ring current merge, and when the tail current is intensified during active times (as measured by *Dst*), this would contribute to an increase in the measured current at midnight. There is insufficient statistics to produce a similar expression for the eastward (inner) ring current, and it is not clear whether one should expect it to move with the westward (outer) current. If it doesn't, this may have interesting implications for the closure of the asymmetric portions of the inner and outer ring current components. *Ijima et al.* [1990], *De Michelis et al.* [1997], and *Nakabe et al.* [1997] each argue for a ring current peak located in the midnight region. Our results as not inconsistent with this notion, as the results that both *Ijima et al.* [1990] and *Nakabe et al.* [1997] quote are for moderately disturbed conditions where we also predict (see Figure 10) the peak to be located tailward of dusk, and since a closer inspection of *Ijima et al.* [1990] appears to show the ring current peak located duskward of midnight. In addition, the results of *De Michelis et al.* [1997] also suggests a duskward of midnight location for the peak, although the results are different to compare directly due to the their use of AE as the state variable.

Recreating *Dst* from the ring current?

The *Dst* index is a measure of the horizontal disturbance created on the ground by all currents in geospace. It has been suggested that there are significant contributions to the *Dst* index from other current systems, such as the cross-tail currents, and the magnetopause currents. Futhermore, it has been suggested that the time variation of these currents make *Dst* a less ideal index for measuring the strength of the ring current.

We will test this hypothesis by computing Dst from the inferred currents shown in Figures 6 and 8. In each spatial bin, i, the ring current is modeled as a circular current loop, with a total current equal to the inferred current density at that point multiplied by the spatial bin's cross-sectional area. The total axial magnetic field at the center of the Earth ($\Delta B_{Z,i}$) given by

$$\Delta B_Z = \sum_i \Delta B_{Z,i}, \tag{9}$$

where

$$\Delta B_{Z,i} = \frac{\mu_0 I , \rho^2}{2 (\rho^2 + z^2)^{3/2}}, \tag{10}$$

where $I = \vec{j} \cdot \delta \vec{A}$.

The results of the computed Dst are shown in Figure 12 as a function of the actual Dst. The solid line shows the computed axial magnetic disturbance created at the origin assuming a non-conducting Earth. We see that as Dst decreases from 0 nT to near -80 nT, so does the computed disturbance at the origin. A thin dashed line showing a one-to-one relationship between the two quantities is shown for comparison. We attribute the large differences at the extreme Dst values to poor statistics. However, in the range of 0 nT to -80 nT the statistics should be sufficient. While the general trend of the computed Dst matches the actual Dst in this range, other unaccounted for factors probably contribute to the different slopes. There are a number of effects that contribute to Dst, and we address two of them next.

First, Dst is derived by taking the difference between a quiet-time baseline magnetic field and the measured magnetic field. This creates an offset since even at quiet times there exists some ring current, and so a Dst of 0 nT corresponds to a ring current that creates some negative perturbation in the main field of the Earth. A second contributing factor is that the Earth is electrically conducting, and that acts to increase the perturbation field at the surface. For a perfectly conducting sphere this increase is 50%. For the Earth values ranging from 30% to 50% are appropriate. If we assume that these are the only two effects causing the solid curve to depart from the dashed line in Figure 12, then their properties can be estimated through a linear fit between the measured Dst and the computed disturbance given by: $Dst = A\,\Delta B_Z + \Delta B_{Z,0}$. Where A is the amplification factor from the conductivity of the Earth and $\Delta B_{Z,0}$ is the quiet-time, baseline Dst offset. The linear fit between -80 and 0 nT yields coefficients of $A = 1.51$, and $\Delta B_{Z,0} = 17.5nT$. The dotted curve in Figure 12 shows the computed magnetic disturbance corrected for a conducting Earth and a baseline offset. This curve, when compared to the dashed line, illustrates the impressive improvement these two straightforward corrections makes to the predicted surface ΔB. If the assumptions of no other contributions are correct, then the conclusion must be that the Earth should be considered a perfectly conducting sphere, and that 17.5 nT should be subtracted from Dst to yield the true disturbance.

Figure 12.

Conclusion

We have constructed an average picture of the westward (outer) and eastward (inner) components of the ring current. We have shown that both components are present for Dst values between -140 nT and 30 nT. The ring current was found to be asymmetric for all Dst, with the peak of the westward (outer) current being located in the afternoon sector during quiet times, and closer to midnight during more disturbed times. An analytic expression for the azimuthal peak of the ring current was given in equation 8, valid for Dst values between -100 and 0 nT. The asymmetry was typically 10-20% for the westward (outer) current, and 15-25% for the eastward (inner) current, using a 12 Hr MLT wide window for comparisons. When using an 8 hour window, the asymmetries increase by approximately 5% points. The pressure peak of the ring current (equivalent to the zero-crossing radius of the azimuthal current) was typically located between 3 and 4 R_E. The radial position of the westward (outer) current moves inward by approximately 0.75 R_E as Dst decreases from 0 nt to -100 nT, while the position of the eastward (inner) current does not move much. We also measured the total current flowing in the westward (outer) and eastward (inner) ring currents as a function of Dst, and found that they vary approximately linearly with Dst, as would be expected. The expression for the total westward (outer) and eastward (inner) currents are given in Eq. 4 and 5 respectively. We finally attempted to reconstruct the Dst perturbation from the measured current patterns. We found a good agreement for Dst values between -80 nT and 0 nT. Linear fits revealed an offset in the Dst index from

the true perturbation by approximately 20 nT, and a correction for induced currents of 50%, corresponding to a perfectly conducting sphere.

Acknowledgment. Work at Los Alamos National Laboratory was conducted under auspice of the U. S. Department of Energy, with partial support from the NASA SR&T programs.

Work at Boston University was supported by NASA grant NAGW-4537 and by NSF grant ATM-9458424.

References

Akasofu, S.-I., and S. Chapman, On the asymmetric development of magnetic storm fields in low and middle latitudes, *Planet. Space Sci.*, *12*, 607–626, 1964.

Chapman, S., An outline of a theory of magnetic storms, *Proc. R. Soc. London, Ser. A*, *95*, 61–83, 1918.

Crooker, N. U., and G. L. Siscoe, A study of the geomagnetic disturbance field asymmetry, *Radio Sci.*, *6*, 495–501, 1971.

Crooker, N. U., and G. L. Siscoe, Birkeland currents as the cause of the low-latitude asymmetric disturbance field, *J. Geophys. Res.*, *1981*, 11,201–11,210, 1981.

De Michelis, P., I. A. Daglis, and G. Consolini, Average terrestrial ring current derived from ampte/cce-chem measurements, *J. Geophys. Res.*, *102*, 14,103–14,111, 1997.

Fejer, J. A., The effects of energetic trapped particles on magnetospheric motions and ionospheric currents, *Can. J. Phys.*, *39*, 1409–1417, 1961.

Harel, M., R. A. Wolf, R. W. Spiro, P. H. Reiff, and C.-K. Chen, Quantitative simulation of a magnetospheric substorm, 2, comparison with observations, *J. Geophys. Res.*, *86*, 2242–2260, 1981.

Ijima, T., T. A. Potemra, and L. J. Zaneti, Large-scale characteristics of magnetospheric equatorial currents, *J. Geophys. Res.*, *95*, 991–999, 1990.

Kirkpatrick, C. B., On current systems proposed for s_d in the theory of magnetic storms, *J. Geophys. Res.*, *57*, 511–526, 1952.

Lui, A. T. Y., and D. C. Hamilton, Radial profiles of quiet time magnetospheric parameters, *J. Geophys. Res.*, *97*, 19,325–19,332, 1992.

Lui, A. T. Y., R. W. McEntire, and S. M. Krimgis, Evolution of the ring current during two gemagnetic storms, *J. Geophys. Res.*, *92*, 7459–7470, 1987.

Mead, G. D., and D. H. Fairfield, A quantitative magnetospheric model derived from spacecraft magnetometer data, *J. Geophys. Res.*, *80*, 523–534, 1975.

Nakabe, S., T. Iyemori, M. Sugiura, and J. A. Slavin, A statistical study of the magnetic field structure in the inner magnetosphere, *J. Geophys. Res.*, *102*, 17,571–17,582, 1997.

Olson, W. P., and K. A. Pfitzer, A quantitative model of the magnetospheric magnetic field, *J. Geophys. Res.*, *79*, 3739–3748, 1974.

Reeves, G. D., L. A. Weiss, M. F. Thomsen, and D. J. McComas, Quantitative experimental verification of the magnetic conjugacy of geosynchronous orbit and the auroral zone, in *Proc. of ICS-3, Versailles, France, 12-17 May 1996*, pp. 579–584, 1996.

Singer, H. J., W. P. Sullivan, P. Anderson, F. Mozer, P. Harvey, J. Wygant, and W. McNeil, Fluxgate magnetometer instrument on the crres, *Journal of Spacecraft and Rockets*, *29*, 599–601, 1992.

Spence, H. E., M. G. Kivelson, and R. J. Walker, Magnetospheric plasma pressure in the midnight meridian: observations from 2.5 to 35 r_e, *J. Geophys. Res.*, *94*, 5264–5272, 1989.

Sugiura, M., B. G. Ledley, T. L. Skillman, and J. P. Heppner, Magnetospheric-field distortions observed by ogo 3 and 5, *J. Geophys. Res.*, *76*, 7552–7565, 1971.

Tsyganenko, N. A., Global quantitative models of the geomagnetic field in the cislunar magetosphere for different disturbance levels, *Planet. Space Sci.*, *35*, 1347–1358, 1987.

Received _____

Draft

This manuscript was prepared with AGU's LaTeX macros v5, with the extension package 'AGU++' by P. W. Daly, version 1.6 from 1999/02/24.

Figure Captions

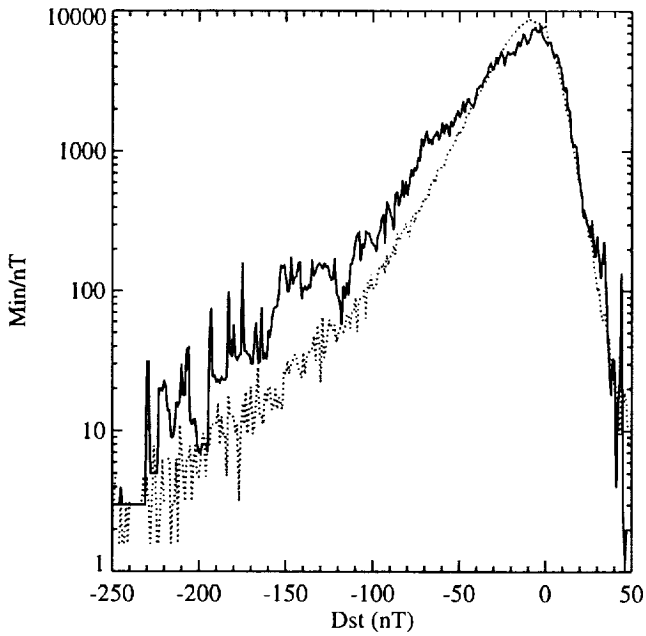

Figure 1. Distribution of the *Dst* index during intervals of good magnetic field measurements (solid), and *Dst* index distribution during the interval January 1, 1970 - December 31, 1996 (dotted, scaled).

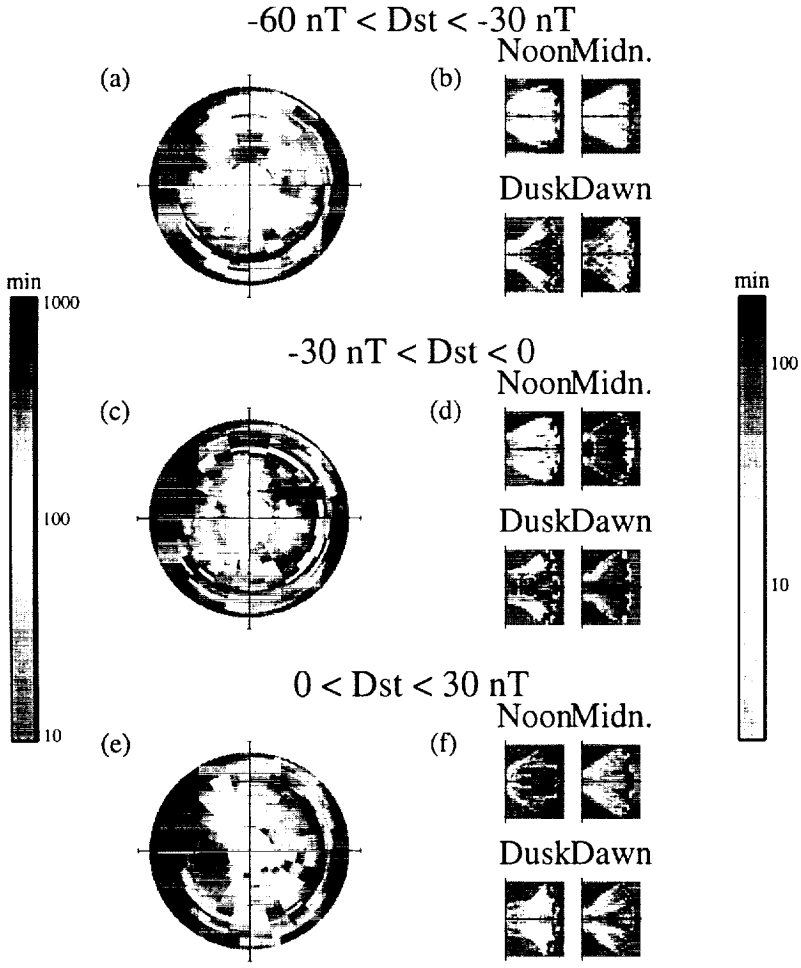

Figure 2. Orbital coverage of CRRES during times when good magnetic field data was taken. The coverage is shown for three *Dst* intervals. Panels a, c, and e show the coverage in L and MLT coordinates plotted as a polar coordinate system. The color scale shows how many minutes CRRES spent in each 0.2 R_E by 1 Hr MLT L-MLT bin. Panels b, d, and f show the coverage in cyllindrical coordinates. Each panel contains four subpanels which show the coverage in the 4 MLT sectors centered at noon, midnight, dusk, and dawn. The color scale shows how many minutes CRRES spent in each 0.2 R_E by 0.2 R_E by 6 Hr MLT bin. As discussed in the text panels b, d, and f contain each data point twice based on a symmetry argument.

Figure Captions

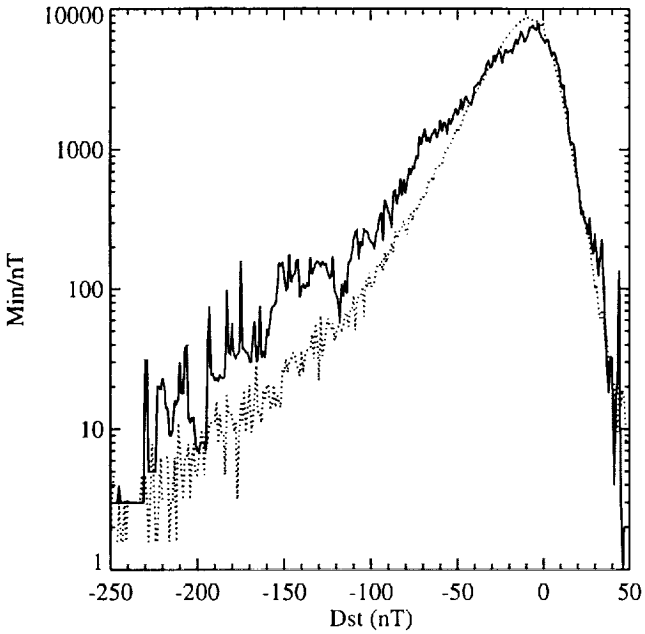

Figure 1. Distribution of the *Dst* index during intervals of good magnetic field measurements (solid), and *Dst* index distribution during the interval January 1, 1970 - December 31, 1996 (dotted, scaled).

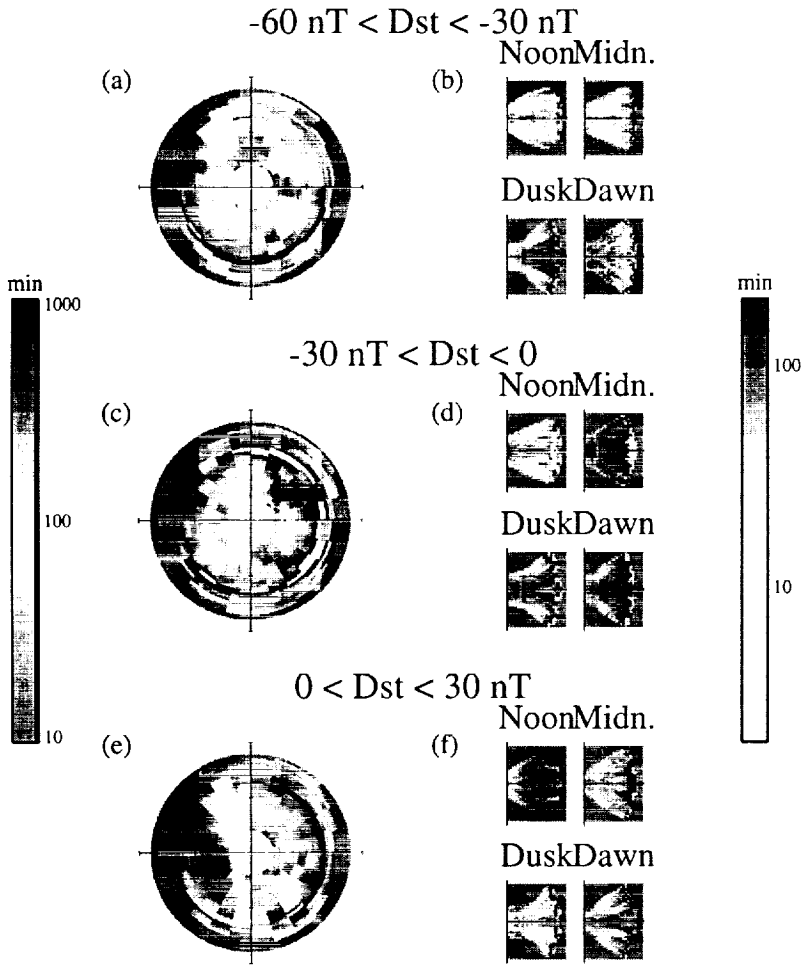

Figure 2. Orbital coverage of CRRES during times when good magnetic field data was taken. The coverage is shown for three *Dst* intervals. Panels a, c, and e show the coverage in L and MLT coordinates plotted as a polar coordinate system. The color scale shows how many minutes CRRES spent in each 0.2 R_E by 1 Hr MLT L-MLT bin. Panels b, d, and f show the coverage in cyllindrical coordinates. Each panel contains four subpanels which show the coverage in the 4 MLT sectors centered at noon, midnight, dusk, and dawn. The color scale shows how many minutes CRRES spent in each 0.2 R_E by 0.2 R_E by 6 Hr MLT bin. As discussed in the text panels b, d, and f contain each data point twice based on a symmetry argument.

Figure Captions

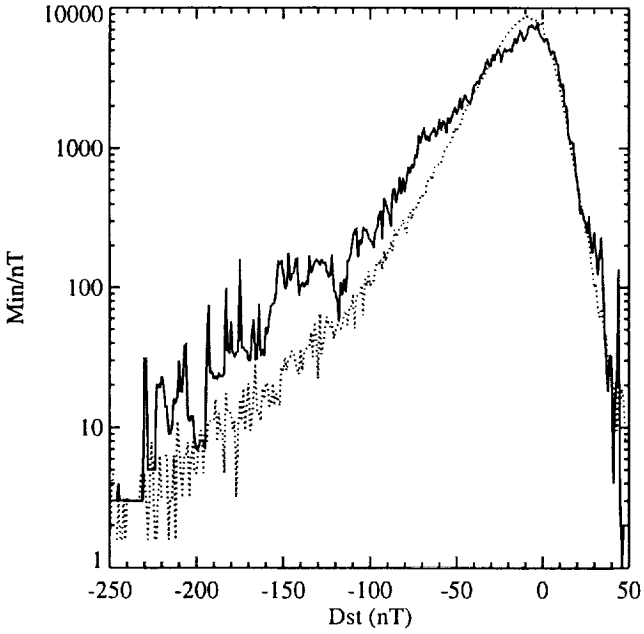

Figure 1. Distribution of the *Dst* index during intervals of good magnetic field measurements (solid), and *Dst* index distribution during the interval January 1, 1970 - December 31, 1996 (dotted, scaled).

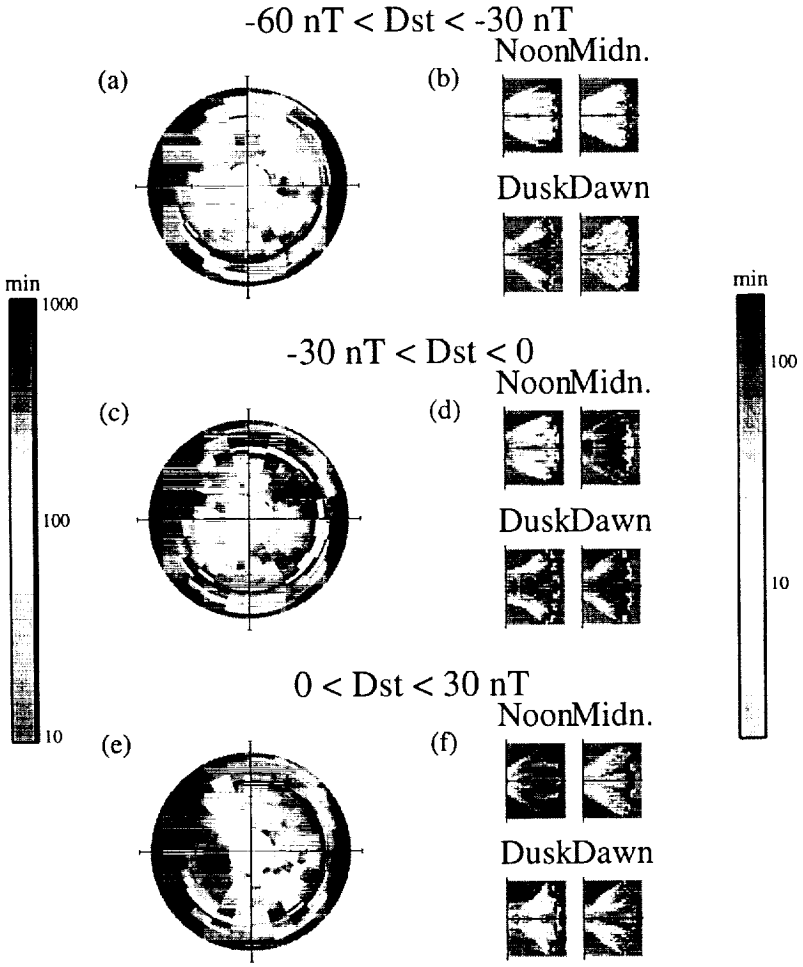

Figure 2. Orbital coverage of CRRES during times when good magnetic field data was taken. The coverage is shown for three *Dst* intervals. Panels a, c, and e show the coverage in L and MLT coordinates plotted as a polar coordinate system. The color scale shows how many minutes CRRES spent in each 0.2 R_E by 1 Hr MLT L-MLT bin. Panels b, d, and f show the coverage in cyllindrical coordinates. Each panel contains four subpanels which show the coverage in the 4 MLT sectors centered at noon, midnight, dusk, and dawn. The color scale shows how many minutes CRRES spent in each 0.2 R_E by 0.2 R_E by 6 Hr MLT bin. As discussed in the text panels b, d, and f contain each data point twice based on a symmetry argument.

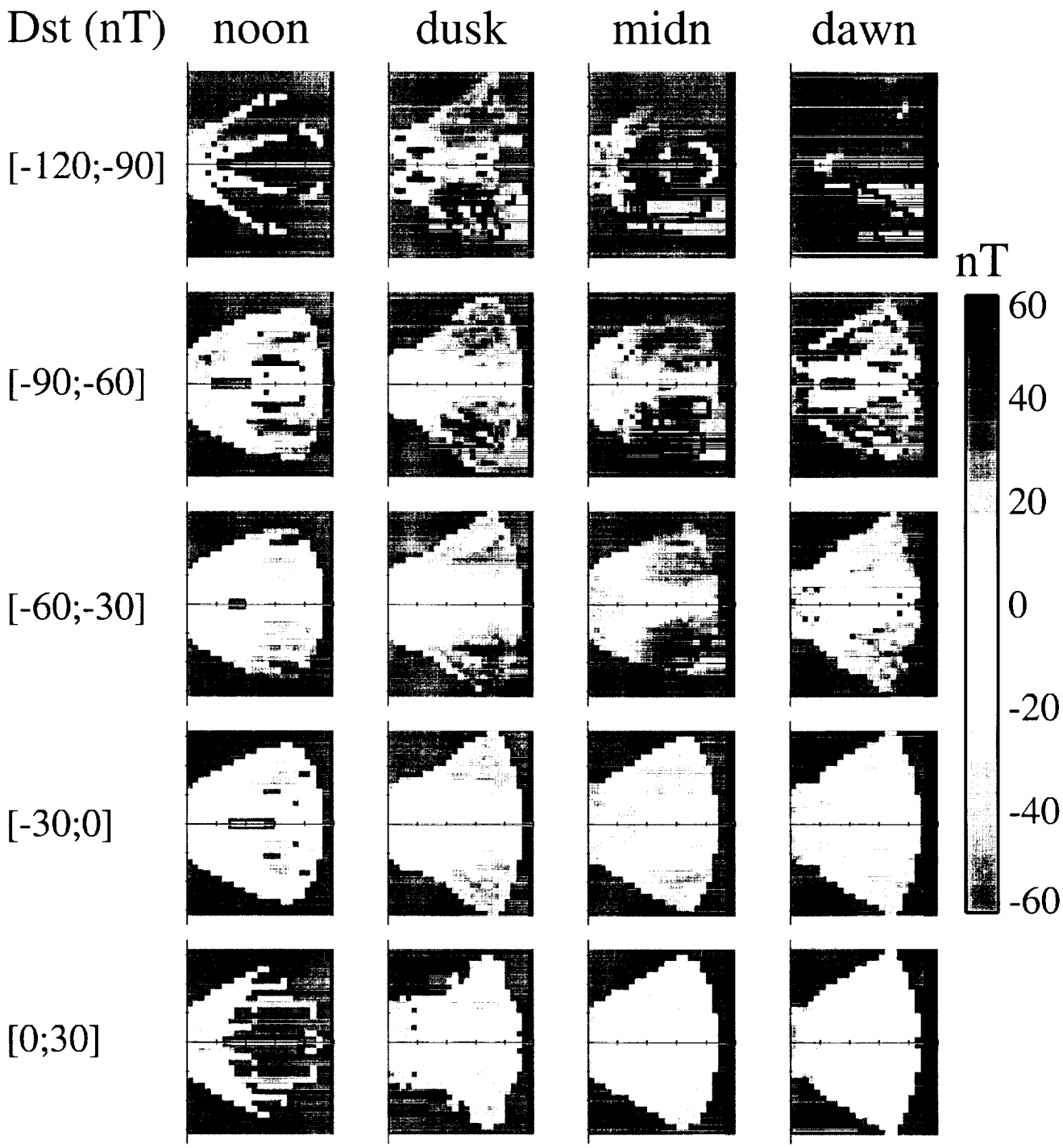

Figure 3. Average radial magnetic field (B_R) for four 6-hour MLT intervals and five *Dst* intervals.

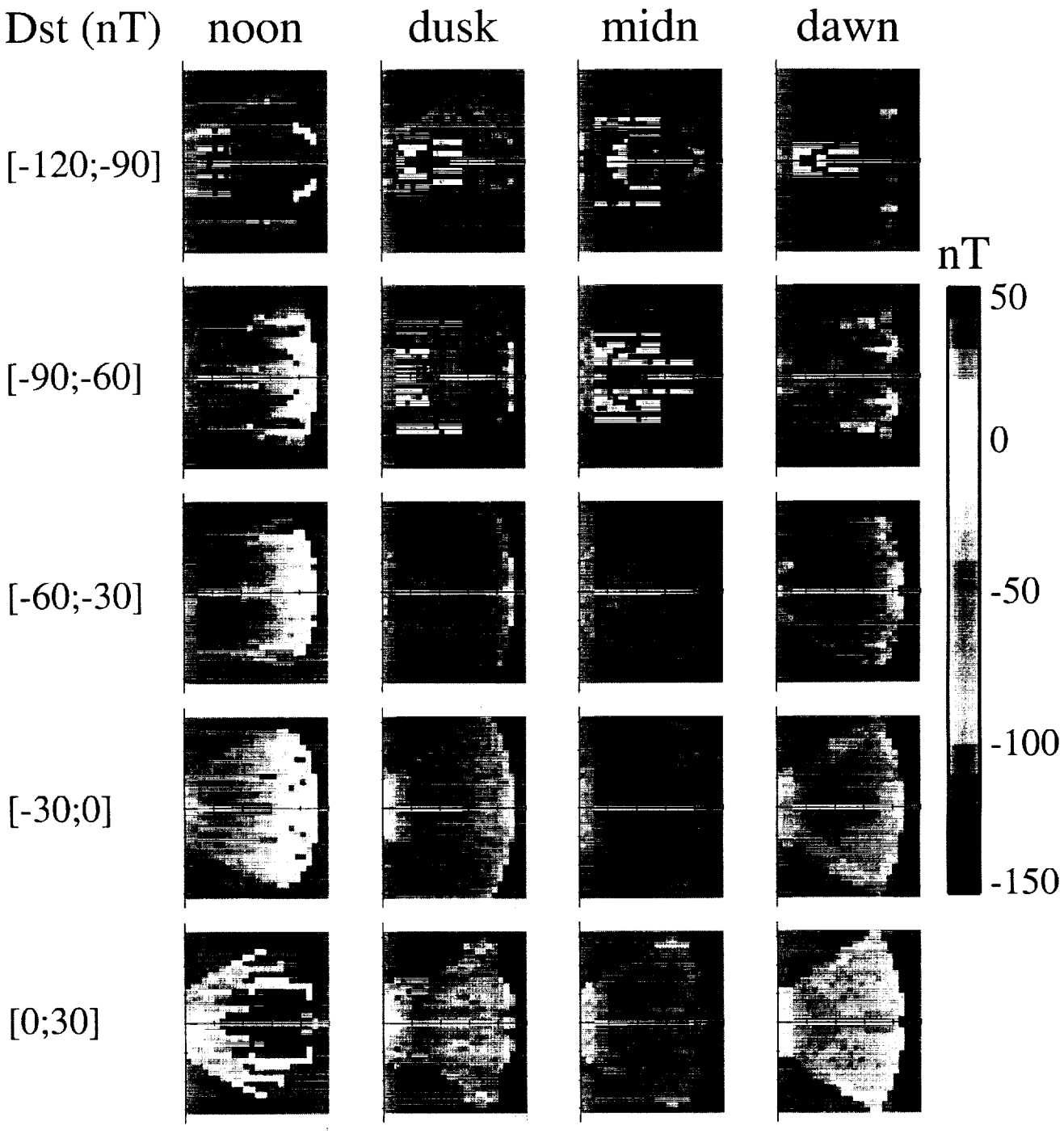

Figure 4. Average axial magnetic field (B_Z) for four 6-hour MLT intervals and five *Dst* intervals.

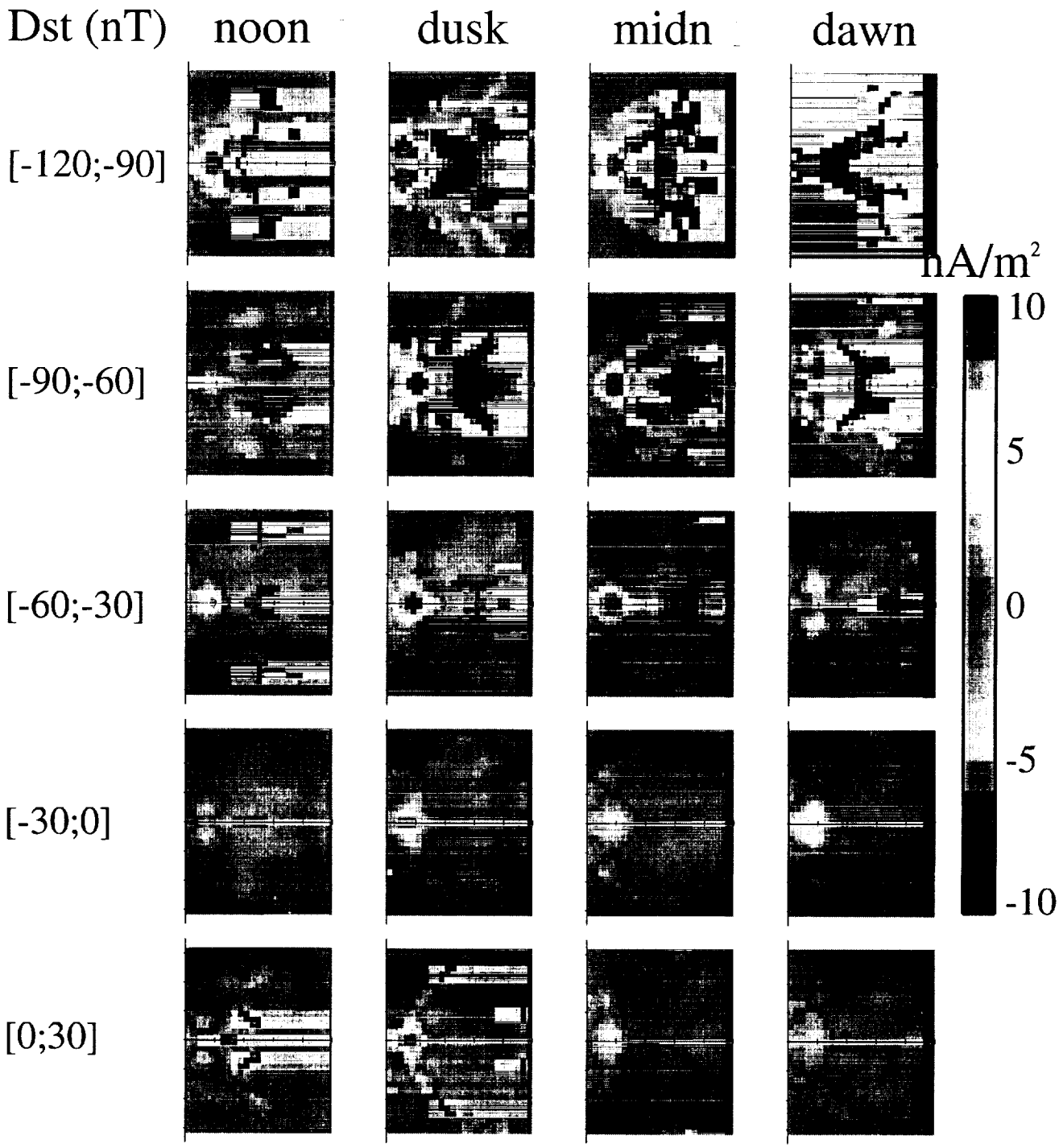

Figure 5. Azimuthal current pattern in the inner magnetosphere calculated using binning in $0.6 \times 0.6\ R_E$ bins separated by $0.2\,R_E$, one smooth, and patching. The currents are for each of four 6-hour local time sectors, and 5 *Dst* intervals. Notice the eastward (inner) component of the ring current in red, and the westward (outer) component of the ring current in blue. Note also, that for lower values of *Dst* - indicating a more intense ring current - the corresponding current patterns appear more intense. Some asymmetry of the ring current is also evident,

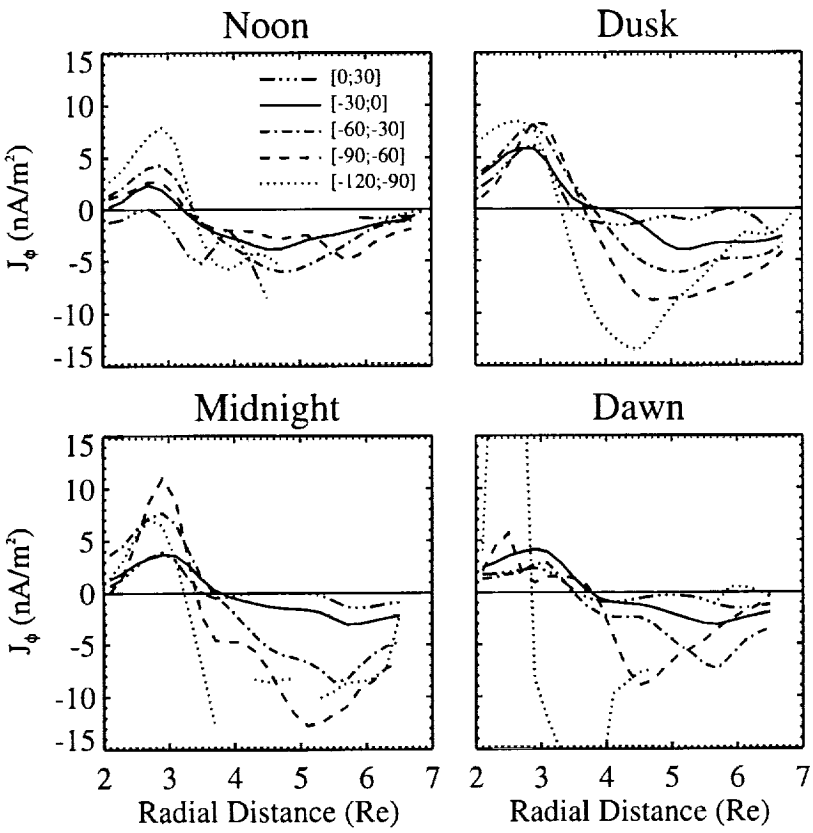

Figure 6. Radial cuts of the equatorial azimuthal current for different *Dst* intervals in differet MLT sectors. Each plot shows the average equatorial azimuthal current as a function of radial distance averaged over $1.2\,R_E$ axially and 6 Hr in MLT. The current densities are larger in the dusk and midnight sectors than in the dawn and noon sectors. Also, the magnitude of the currents increase with decreasing *Dst*. The westward (outer) component exhibits a larger variation of the current density with *Dst* than the eastward (inner) component.

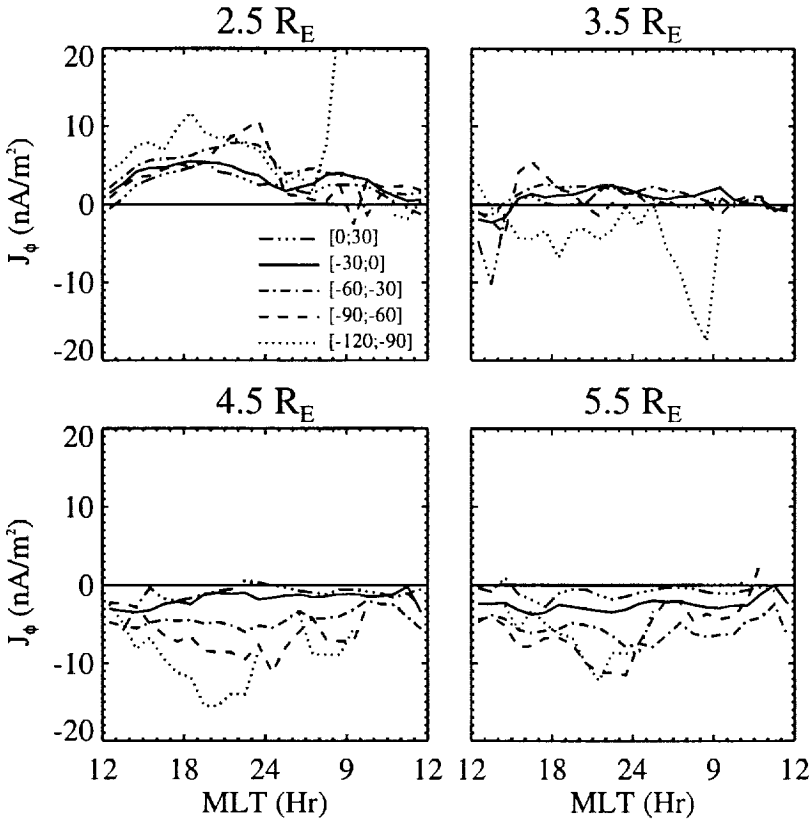

Figure 7. MLT cuts of the equatorial azimuthal current for 4 different radial intervals. In each plot is shown the average equatorial azimuthal current as a function of MLT at 1 hour intervals, and in 1 R_E radial by 1.2 R_E axial, by 4 Hr MLT bins.

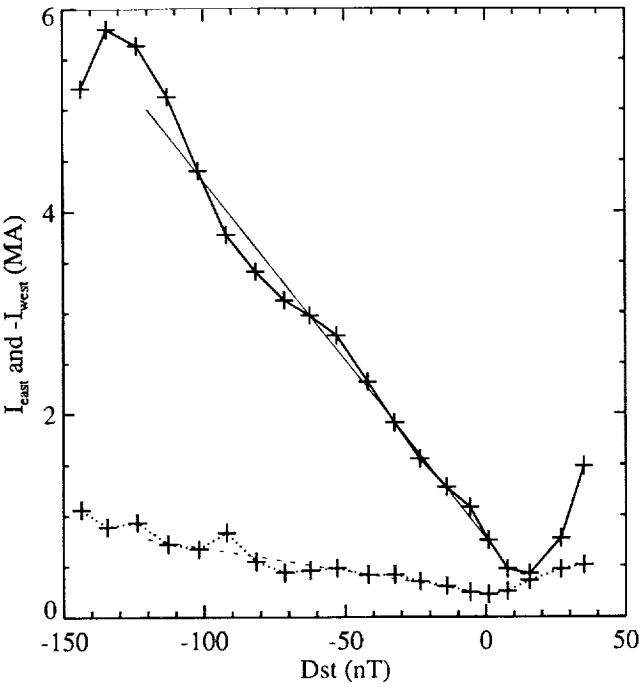

Figure 8. Total current in the ring current region as a function of the *Dst* index. The total westward (outer) current is plotted as a solid line, while the total eastward (inner) current is plotted as a dotted line. The currents are plotted as a function of the average *Dst* in each 30 nT wide bin. The straight lines represent fits to the current density.

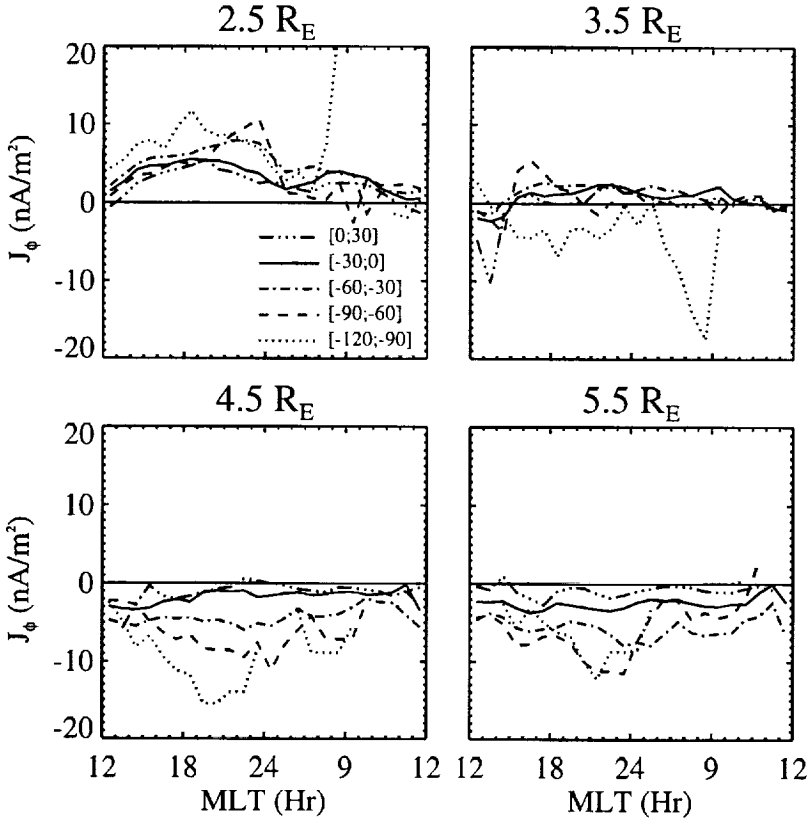

Figure 7. MLT cuts of the equatorial azimuthal current for 4 different radial intervals. In each plot is shown the average equatorial azimuthal current as a function of MLT at 1 hour intervals, and in 1 R_E radial by 1.2 R_E axial, by 4 Hr MLT bins.

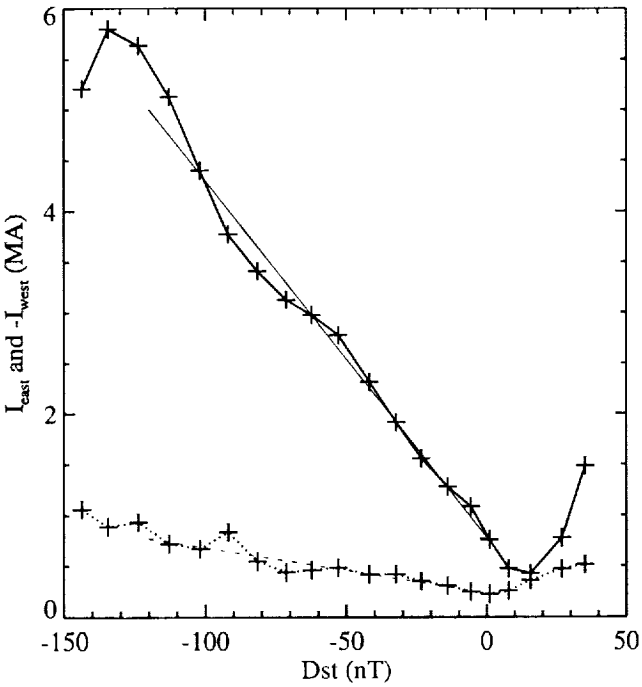

Figure 8. Total current in the ring current region as a function of the *Dst* index. The total westward (outer) current is plotted as a solid line, while the total eastward (inner) current is plotted as a dotted line. The currents are plotted as a function of the average *Dst* in each 30 nT wide bin. The straight lines represent fits to the current density.

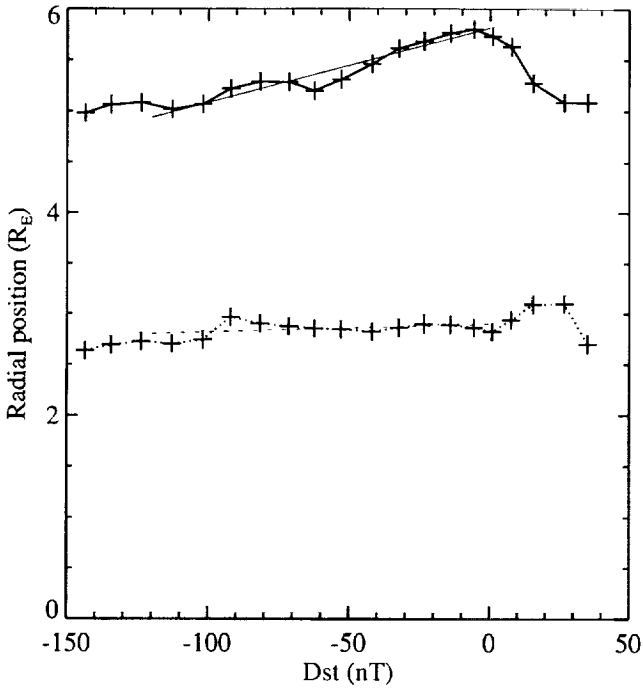

Figure 9. Weighted average location of the westward (outer) and eastward (inner) ring currents as a function of *Dst*. The thick solid line is the position of the westward (outer) current, and the thick dotted line is the position of the eastward (inner) current. The straight thin lines represent linear fits. It can be seen that the westward (outer) current moves significatly inwards as *Dst* decreases, whereas the eastward (inner) current only moves slightly inwards.

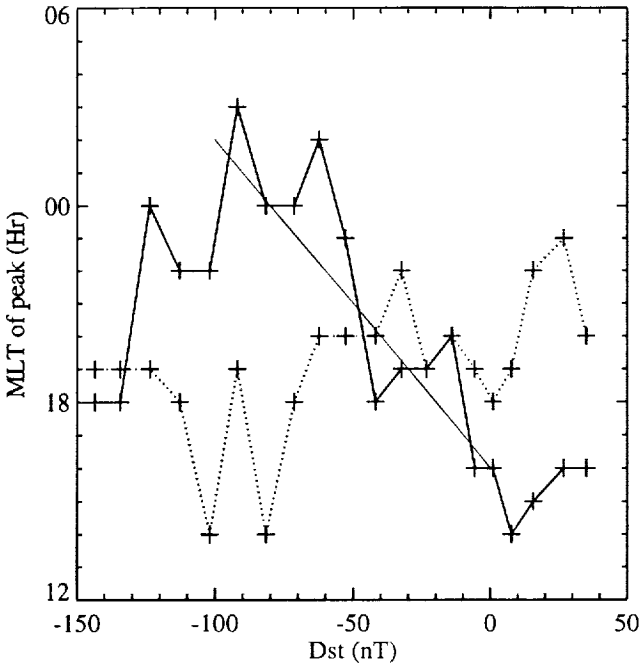

Figure 10. Position of the asymmetry peak of the ring current density as a function of *Dst*. The solid line shows the asymmetry of the westward (outer) current, while the dotted line shows the asymmetry of the eastward (inner) current. The thin solid line shows a linear expression that approximates the progression of the asymmetry peak as a function of *Dst*.

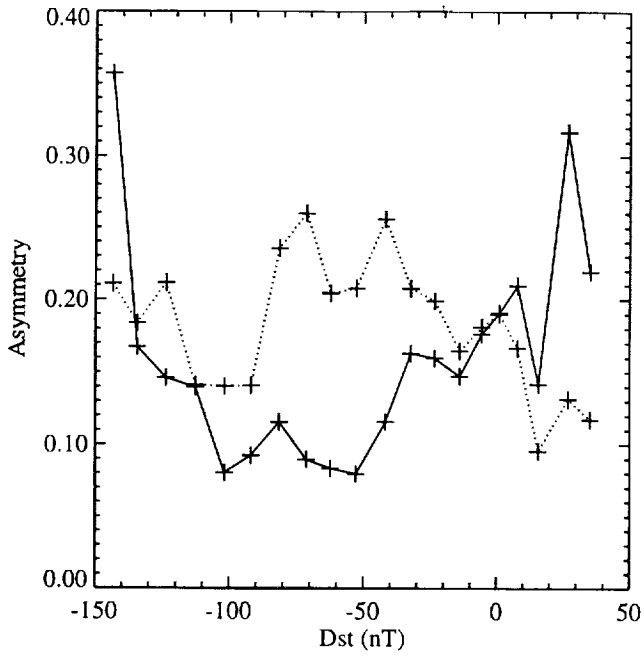

Figure 11. 12 hour MLT averaged asymmetry of the ring current. The solid line shows the asymmetry of the westward (outer) current, and the dotted line shows the asymmetry of the eastward (inner) current.

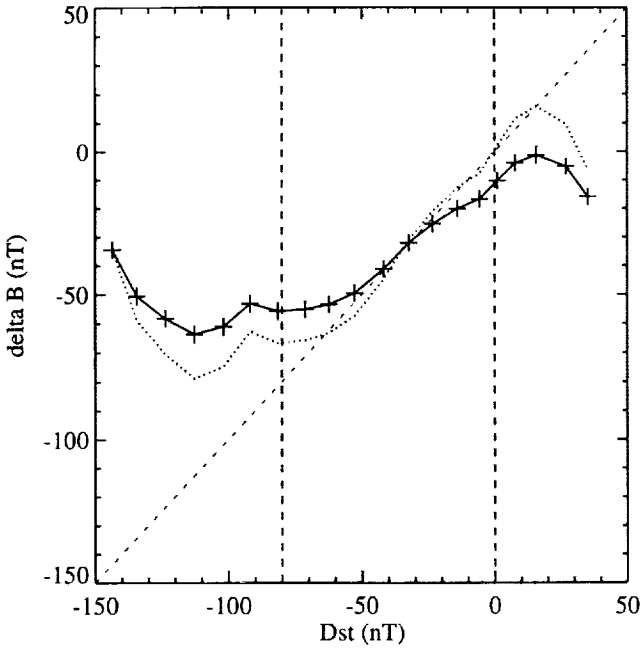

Figure 12. Ground magnetic disturbance reconstructed from the same ring current patterns used to create Figure 8. The solid line shows the magnetic disturbance due to the ring current for a non-conducting Earth. The dotted line shows the magnetic disturbance corrected for a conducting Earth and for a zero offset in the *Dst* index.

Tables

Interval	Time	Fraction
nT	Min	%
< -120	7147	2.0
-120 to -90	6372	1.8
-90 to -60	25300	7.0
-60 to -30	71167	20
-30 to 0	174718	49
0 to 30	73180	20
≥ 30	1407	0.39
All	359291	100

Table 1. The number of measurements occurring in different *Dst* ranges. Many measurements fall in the 30 nT wide bins between -90 and 30 nT, but outside that interval the statistics drop off rapidly.

Dst	L-MLT		R-ϕ-Z	
nT	Avg.	Med.	Avg.	Med.
−120 to −90	23	14	12	8
−90 to −60	58	33	22	15
−60 to −30	135	80	45	31
−30 to 0	323	225	101	76
0 to 30	143	93	52	35

Table 2. Average and median residence times per bin in which the residence time was at least 1 minute. In columns two and three, the median and average residence time in each L-shell, MLT bin of dimension 0.25 R_E by 1 Hr MLT bin between L of 2 and 9 R_E. In columns 4 and 5 are shown the average residence time in each bin in cyllindrical coordinates, 0.2 R_E by 1 Hr MLT by 0.2 R_E between 2 and 7 R_E cyllindrical radius, and −3.2 and 3.2 R_E axial distance.